Icarus 281 (2017) 103–114

Contents lists available at ScienceDirect

Icarus

journal homepage: www.elsevier.com/locate/icarus

Low surface gravitational acceleration of Mars results in a thick and weak lithosphere: Implications for topography, volcanism, and hydrology

Michael J. Heap[a,*], Paul K. Byrne[b], Sami Mikhail[c]

[a] Géophysique Expérimentale, Institut de Physique de Globe de Strasbourg (UMR 7516 CNRS, Université de Strasbourg/EOST), 5 rue René Descartes, Cedex 67084 Strasbourg, France
[b] Planetary Research Group, Department of Marine, Earth, and Atmospheric Sciences, North Carolina State University, Raleigh, North Carolina, USA
[c] The Department of Earth and Environmental Sciences, School of Geography and Geosciences, Irvine Building, The University of St Andrews, UK

ARTICLE INFO

Article history:
Available online 10 September 2016

Keywords:
Mars
Brittle
Ductile
Volcano
Dyke
Lithosphere
Strength

ABSTRACT

Surface gravitational acceleration (surface gravity) on Mars, the second-smallest planet in the Solar System, is much lower than that on Earth. A direct consequence of this low surface gravity is that lithostatic pressure is lower on Mars than on Earth at any given depth. Collated published data from deformation experiments on basalts suggest that, throughout its geological history (and thus thermal evolution), the Martian brittle lithosphere was much thicker but weaker than that of present-day Earth as a function solely of surface gravity. We also demonstrate, again as a consequence of its lower surface gravity, that the Martian lithosphere is more porous, that fractures on Mars remain open to greater depths and are wider at a given depth, and that the maximum penetration depth for opening-mode fractures (i.e., joints) is much deeper on Mars than on Earth. The result of a weak Martian lithosphere is that dykes—the primary mechanism for magma transport on both planets—can propagate more easily and can be much wider on Mars than on Earth. We suggest that this increased the efficiency of magma delivery to and towards the Martian surface during its volcanically active past, and therefore assisted the exogeneous and endogenous growth of the planet's enormous volcanoes (the heights of which are supported by the thick Martian lithosphere) as well as extensive flood-mode volcanism. The porous and pervasively fractured (and permeable) nature of the Martian lithosphere will have also greatly assisted the subsurface storage of and transport of fluids through the lithosphere throughout its geologically history. And so it is that surface gravity, influenced by the mass of a planetary body, can greatly modify the mechanical and hydraulic behaviour of its lithosphere with manifest differences in surface topography and geomorphology, volcanic character, and hydrology.

1. Introduction

Despite their similar bulk composition (McSween et al., 2009) and proximity in the Solar System, there are significant differences between present-day Earth and Mars. First, although the water-carved Martian landscape suggests that large bodies of liquid water existed on Mars in the geological past, water on the now dusty Martian surface (Wang and Richardson, 2015) is largely restricted to polar ice (Carr and Head, 2010; 2015) and seasonal brines (Martín-Torres et al., 2015; Ojha et al., 2015). By contrast, two-thirds of the surface of Earth is covered by liquid water. The surface atmospheric composition (Owen et al., 1977), atmospheric pressure (Tillman et al., 1993), and average temperature (Kieffer et al., 1977) of Earth and Mars also differ substantially. Further, the surface of Mars exhibits a hypsometric distribution with a substantially higher mean and variance than Earth (Smith et al., 1999; Zuber et al., 2000; Aharonson et al., 2001): west of the Tharsis volcanic plateau lies the tallest known volcano in the Solar System, Olympus Mons (with 22 km of relief; Plescia, 2004), and there is a marked contrast (~5.5 km) between the average elevation of the northern and southern hemisphere of Mars, known as the Martian dichotomy (McGill and Squyres, 1991; Smith and Zuber, 1996; Watters et al., 2007). There are several pronounced differences in the volcanic character of Mars and Earth (Carr, 1973; Greely and Spudis, 1981; Wilson and Head, 1983, 1994; Wilson, 2009). The most noteworthy difference is that although 90% of magmatism on Earth occurs along the curvilinear belts that define plate tec-

* Corresponding author.
E-mail address: heap@unistra.fr (M.J. Heap).

http://dx.doi.org/10.1016/j.icarus.2016.09.003
0019-1035/

tonic boundaries (Crisp, 1984; Cottrell, 2015), Mars is a one-plate planet (Solomon, 1978) and therefore magmatism on Mars is almost exclusively defined as intra-plate (Wilson, 2009). However, the stagnant-lid tectonic regime on Mars prohibits the formation of the volcanic island chains that typify intra-plate volcanism on Earth (e.g., Hawaii; Morgan, 1972).

The considerable present-day differences between Earth and Mars are a reflection of their very different geological histories. Although the reasons for such contrasts are many, we explore here the contribution of one of the most striking differences between Earth and Mars: their considerable difference in radius, and therefore mass. Specifically, we tackle the influence of the resultant difference in surface gravitational acceleration gravity (hereafter called surface gravity) on the mechanical and hydraulic behaviour of the Martian lithosphere. To do so, we interrogate the wealth of published experimental rock deformation data on basalt (and diabase), a database that has increased greatly over the last decade. With these data, we discuss the implications of the low Martian surface gravity for surface topography and geomorphology, volcanic character, and hydrology. We restrict our discussion to differences between Earth and Mars, but the implications discussed herein also apply to a wide range of planetary bodies in the Solar System and beyond with a basaltic (or mechanical cognate) primary crustal lithology (from small planetary bodies with a low surface gravity such as the Moon to telluric super-Earths with very large surface gravities).

2. The influence of surface gravitational acceleration

The surface gravity g of a planet plays a controlling role in the magnitude of lithostatic pressure at a given depth. Because of the low surface gravity of Mars with respect to Earth (9.807 m/s^2 and 3.711 m/s^2, respectively), the pressure at a given depth on Mars will be substantially lower than on Earth. For a constant bulk density ρ of 2900 kg/m^3, the lithostatic pressure P at a depth z of 1000 m is ~28 and ~11 MPa for Earth and Mars, respectively, where $P = \rho gz$. Importantly, lithostatic pressure exerts a first-order control on the mechanical and hydraulic behaviour of rock. First, low lithostatic pressure favours a brittle mode of failure (Paterson and Wong, 2005; Wong and Baud, 2012); lower surface gravity will therefore increase the depth of the brittle–ductile transition (BDT) (i.e., it will increase the thickness of the brittle lithosphere). Second, the strength (i.e., the resistance to failure) of rock in the brittle field is reduced as lithostatic pressure decreases (Paterson and Wong, 2005). For example, the compressive strength (i.e., the maximum compressive stress σ_p a rock sample can withstand before macroscopic failure; see Fig. 1) of low-porosity basalt from Mt Etna (Italy) is 504 MPa at an effective pressure of 50 MPa, which corresponds to a depth of ~2 km on Earth and ~5 km on Mars; this strength is reduced to 291 MPa at an effective pressure of 10 MPa, a depth of ~0.4 km on Earth and ~1 km on Mars (Heap et al., 2011). Next, the fracture density and the average fracture aperture will be greater at lower lithostatic pressures because micro- and macrofractures readily close as lithostatic pressure increases (Vinciguerra et al., 2005; Nara et al., 2011). Crucially, an increase in fracture density (Mitchell and Faulkner, 2012) and/or aperture (Zimmerman and Bodvarsson, 1996) can greatly increase rock permeability, a material property that plays a fundamental role in the distribution and magnitude of pore pressures within the lithosphere (David et al., 1994). Finally, Griffith failure theory predicts that the maximum depth of downward-propagating opening-mode (i.e., Mode I) fractures will increase as surface gravity decreases (Gudmundsson, 2011). We discuss these consequences in turn below.

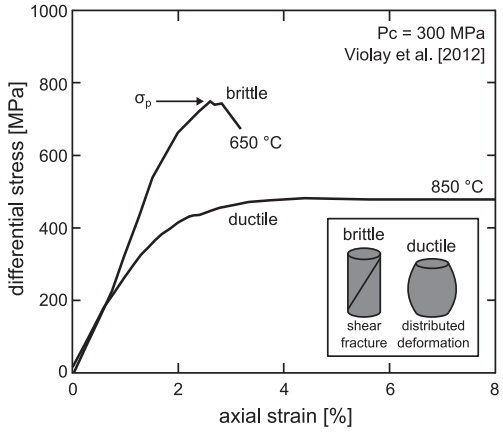

Fig. 1. The mechanical behaviour of rock in compression. Examples of brittle and ductile stress–strain curves for basalt deformed at a confining pressure of 300 MPa and a temperature of 650 °C (brittle test) and 850 °C (ductile test) (data from Violay et al., 2012). Inset shows cartoons depicting post-failure samples typical of brittle (throughgoing shear fracture) and ductile (distributed deformation) deformation.

2.1. Influence of surface gravity on the depth of the brittle–ductile transition (BDT)

Many laboratory deformation experiments have shown that pressure and temperature can modify the failure mode of material. Low and high pressure and/or temperature are typically synonymous with brittle and ductile behaviour, respectively (Evans et al., 1990; Paterson and Wong, 2005; Wong and Baud, 2012). Since the majority of the Terran and Martian lithospheres are basaltic in composition (McSween et al., 2009), we have compiled published high-temperature experimental rock deformation data for basaltic rocks (including diabase) over a wide range of pressures (Table 1), with which we then use to provide an approximate depth interval for the BDT on Earth and Mars. We interpret the BDT as a purely mechanical boundary that can be estimated by observing the failure mode (brittle or ductile) of rock during deformation experiments. A limitation of this approach is that laboratory strain rates (~10^{-5} s^{-1}) are much higher than typical real-world strain rates (strain rates on Mars are typically considered to be between 10^{-19} and 10^{-16} s^{-1}; McGovern et al., 2002; Wilkins et al., 2002). However, we note that (1) experiments already classed as ductile at laboratory strain rates will remain ductile at lower strain rates and, (2) lowering the strain rate at low-pressure and low-temperature will reduce rock strength—due to the increased time available for subcritical crack growth (Brantut et al., 2013)—but may not necessarily promote ductility. For example, the experiments of Heap et al. (2011) show that basalt can deform in a brittle manner at a strain rate of 10^{-9} s^{-1}. Additionally, although the failure mode of volcanic rocks with a significant glass phase is sensitive to strain rate at temperatures above their appropriate glass transition temperature (Lavallée et al., 2013), basalts (that typically contain a subordinate glass phase) are much less sensitive to such changes.

The compiled rock deformation experiments (Table 1) were performed on cylindrical samples (typically between 20 and 50 mm in diameter) in either a triaxial (i.e., with a confining pressure) or uniaxial (i.e., without a confining pressure) deformation apparatus. Samples were deformed in compression in all cases. Although most experiments were conducted at a constant strain rate (in which an axial piston moves at a constant displacement rate to deform the sample), typically between 10^{-6} and 10^{-4} s^{-1}, select experiments were performed under an imposed constant stress (creep tests) (e.g., Mackwell et al., 1998; Heap et al., 2011). Samples in the

Table 1
Summary of the experimental conditions for the rock deformation experiments used in this study (for the construction of Figs. 3–5). *Pc* = confining pressure; *Pp* = pore fluid pressure; *Peff* = effective pressure; *T* = experimental temperature; σ_p = peak differential stress (see Fig. 1). In some cases, failure mode classification differs from that stated in the original publication. Data not included in this compilation are uniaxial experiments conducted at room temperature and instances of non-viscous ductile deformation. φ = porosity.

Reference	*Pc* (MPa)	*Pp* (MPa)	*Peff* (MPa)	*T* (°C)	σ_p (MPa)	Failure mode	Notes
Griggs et al. (1960)	500	0	500	25	1668	Brittle	Basalt
Griggs et al. (1960)	500	0	500	300	1390	Brittle	Basalt
Griggs et al. (1960)	500	0	500	500	1080	Brittle	Basalt
Griggs et al. (1960)	500	0	500	700	–	Ductile	Basalt
Griggs et al. (1960)	500	0	500	800	–	Ductile	Basalt
Caristan (1982)	0	0	0	950	199	Brittle	Maryland diabase; strain rate = 10^{-3} s^{-1}
Caristan (1982)	0	0	0	970	223	Brittle	Maryland diabase; strain rate = 10^{-5} s^{-1}
Caristan (1982)	0	0	0	995	193	Brittle	Maryland diabase; strain rate = 10^{-3} s^{-1}
Caristan (1982)	30	0	30	1000	370	Brittle	Maryland diabase; strain rate = 10^{-3} s^{-1}
Caristan (1982)	50	0	50	1000	440	Brittle	Maryland diabase; strain rate = 10^{-3} s^{-1}
Caristan (1982)	150	0	150	810	780	Brittle	Maryland diabase; strain rate = 10^{-6} s^{-1}
Caristan (1982)	150	0	150	970	385	Brittle	Maryland diabase; strain rate = 10^{-6} s^{-1}
Caristan (1982)	150	0	150	994	535	Brittle	Maryland diabase; strain rate = 10^{-3} s^{-1}
Caristan (1982)	150	0	150	1000	566	Brittle	Maryland diabase; strain rate = 10^{-4} s^{-1}
Caristan (1982)	150	0	150	1000	561	Brittle	Maryland diabase; strain rate = 10^{-5} s^{-1}
Caristan (1982)	150	0	150	1000	573	Brittle	Maryland diabase; strain rate = 10^{-5} s^{-1}
Caristan (1982)	350	0	350	1000	–	Ductile	Maryland diabase; strain rate = 10^{-5} s^{-1}
Caristan (1982)	400	0	400	1000	–	Ductile	Maryland diabase; strain rate = 10^{-4} s^{-1}
Caristan (1982)	425	0	425	1000	–	Ductile	Maryland diabase; strain rate = 10^{-4} s^{-1}
Caristan (1982)	425	0	425	1000	–	Ductile	Maryland diabase; strain rate = 10^{-5} s^{-1}
Caristan (1982)	425	0	425	1000	–	Ductile	Maryland diabase; strain rate = 10^{-6} s^{-1}
Caristan (1982)	450	0	450	1000	–	Ductile	Maryland diabase; strain rate = 10^{-5} s^{-1}
Shimada and Yukutake (1982)	57	0	57	25	400	Brittle	Yakuno basalt; φ = 0.07; strain rate = 10^{-5} s^{-1}
Shimada and Yukutake (1982)	107	0	107	25	415	Brittle	Yakuno basalt; φ = 0.07; strain rate = 10^{-5} s^{-1}
Bauer et al. (1981)	50	0	50	25	540	Brittle	Cuerbio basalt; φ = 0.05–0.08; strain rate = 10^{-4} s^{-1}
Bauer et al. (1981)	50	0	50	25	400	Brittle	Cuerbio basalt; φ = 0.05–0.08; strain rate = 10^{-4} s^{-1}
Bauer et al. (1981)	50	0	50	600	300	Brittle	Cuerbio basalt; φ = 0.05–0.08; strain rate = 10^{-4} s^{-1}
Bauer et al. (1981)	50	0	50	600	340	Brittle	Cuerbio basalt; φ = 0.05–0.08; strain rate = 10^{-4} s^{-1}
Bauer et al. (1981)	50	0	50	700	300	Brittle	Cuerbio basalt; φ = 0.05–0.08; strain rate = 10^{-4} s^{-1}
Bauer et al. (1981)	50	0	50	940	125	Brittle	Cuerbio basalt; φ = 0.05–0.08; strain rate = 10^{-4} s^{-1}
Bauer et al. (1981)	50	0	50	940	200	Brittle	Cuerbio basalt; φ = 0.05–0.08; strain rate = 10^{-4} s^{-1}
Bauer et al. (1981)	50	0	50	1000	100	Brittle	Cuerbio basalt; φ = 0.05–0.08; strain rate = 10^{-4} s^{-1}
Bauer et al. (1981)	100	0	100	700	465	Brittle	Cuerbio basalt; φ = 0.05–0.08; strain rate = 10^{-4} s^{-1}
Bauer et al. (1981)	100	0	100	900	240	Brittle	Cuerbio basalt; φ = 0.05–0.08; strain rate = 10^{-4} s^{-1}
Bauer et al. (1981)	100	0	100	950	110	Brittle	Cuerbio basalt; φ = 0.05–0.08; strain rate = 10^{-4} s^{-1}
Bauer et al. (1981)	100	0	100	1000	180	Brittle	Cuerbio basalt; φ = 0.05–0.08; strain rate = 10^{-4} s^{-1}
Bauer et al. (1981)	100	50	50	820	180	Brittle	Cuerbio basalt; φ = 0.05–0.08; strain rate = 10^{-4} s^{-1}
Shimada 1986	57	0	57	25	410	Brittle	Yakuno basalt; φ = 0.07; strain rate = 10^{-5} s^{-1}
Duclos and Paquet 1991	0	0	0	300	399	Brittle	Alkaline basalt; partially glassy; strain rate = 10^{-6} s^{-1}
Duclos and Paquet 1991	0	0	0	600	430	Brittle	Alkaline basalt; partially glassy; strain rate = 10^{-6} s^{-1}
Duclos and Paquet 1991	0	0	0	700	445	Brittle	Alkaline basalt; partially glassy; strain rate = 10^{-6} s^{-1}
Duclos and Paquet 1991	0	0	0	750	430	Brittle	Alkaline basalt; partially glassy; strain rate = 10^{-6} s^{-1}
Duclos and Paquet 1991	0	0	0	800	–	Ductile	Alkaline basalt; partially glassy; strain rate = 10^{-6} s^{-1}
Duclos and Paquet 1991	0	0	0	900	–	Ductile	Alkaline basalt; partially glassy; strain rate = 10^{-6} s^{-1}
Duclos and Paquet 1991	0	0	0	1000	–	Ductile	Alkaline basalt; partially glassy; strain rate = 10^{-6} s^{-1}
Hacker and Christie 1991	1000	0	1000	675	–	Ductile	Tholeiitic basalt; partially glassy; 0.5 wt.% water added; strain rate = 10^{-4}–10^{-7} s^{-1}
Hacker and Christie 1991	1000	0	1000	725	–	Ductile	Tholeiitic basalt; partially glassy; 0.5 wt.% water added; strain rate = 10^{-4}–10^{-7} s^{-1}
Hacker and Christie 1991	1000	0	1000	775	–	Ductile	Tholeiitic basalt; partially glassy; 0.5 wt.% water added; strain rate = 10^{-4}–10^{-7} s^{-1}
Hacker and Christie 1991	1000	0	1000	825	–	Ductile	Tholeiitic basalt; partially glassy; 0.5 wt.% water added; strain rate = 10^{-4}–10^{-7} s^{-1}
Hacker and Christie 1991	1000	0	1000	875	–	Ductile	Tholeiitic basalt; partially glassy; 0.5 wt.% water added; strain rate = 10^{-4}–10^{-7} s^{-1}
Schultz 1993	0	0	0	450	210	Brittle	Estimated strength value taken as 80% of the average uniaxial compressive strength for basalt; see Schultz (1993) for details
Mackwell et al. (1998)	400	0	400	1000	–	Ductile	Dehydrated Maryland and Columbia diabase; creep test; strain rate = 10^{-5}–10^{-7} s^{-1}
Mackwell et al. (1998)	400	0	400	1050	–	Ductile	Dehydrated Maryland and Columbia diabase; creep test; strain rate = 10^{-5}–10^{-7} s^{-1}
Mackwell et al. (1998)	400	0	400	1050	–	Ductile	Dehydrated Maryland and Columbia diabase; creep test; strain rate = 10^{-5}–10^{-7} s^{-1}
Mackwell et al. (1998)	450	0	450	970	–	Ductile	Dehydrated Maryland and Columbia diabase; creep test; strain rate = 10^{-5}–10^{-7} s^{-1}
Mackwell et al. (1998)	450	0	450	1000	–	Ductile	Dehydrated Maryland and Columbia diabase; creep test; strain rate = 10^{-5}–10^{-7} s^{-1}

(*continued on next page*)

Table 1 (*continued*)

Reference	*Pc* (MPa)	*Pp* (MPa)	*Peff* (MPa)	*T* (°C)	σ_p (MPa)	Failure mode	Notes
Mackwell et al. (1998)	450	0	450	1050	–	Ductile	Dehydrated Maryland and Columbia diabase; creep test; strain rate = 10^{-5}–10^{-7} s^{-1}
Mackwell et al. (1998)	500	0	500	1000	–	Ductile	Dehydrated Maryland and Columbia diabase; creep test; strain rate = 10^{-5}–10^{-7} s^{-1}
Rocchi et al. (2004)	0	0	0	300	89	Brittle	Vesuvius basalt; φ = 0.08–0.10; strain rate = 10^{-5} s^{-1}
Rocchi et al. (2004)	0	0	0	300	104	Brittle	Etna "core" basalt; strain rate = 10^{-5} s^{-1}
Rocchi et al. (2004)	0	0	0	300	35	Brittle	Etna "crust" basalt; strain rate = 10^{-5} s^{-1}
Rocchi et al. (2004)	0	0	0	600	96	Brittle	Vesuvius basalt; φ = 0.08–0.10; strain rate = 10^{-5} s^{-1}
Rocchi et al. (2004)	0	0	0	600	105	Brittle	Vesuvius basalt; φ = 0.08–0.10; strain rate = 10^{-5} s^{-1}
Rocchi et al. (2004)	0	0	0	600	103	Brittle	Etna "core" basalt; strain rate = 10^{-5} s^{-1}
Rocchi et al. (2004)	0	0	0	600	181	Brittle	Etna "core" basalt; strain rate = 10^{-5} s^{-1}
Rocchi et al. (2004)	0	0	0	600	40.5	Brittle	Etna "crust" basalt; strain rate = 10^{-5} s^{-1}
Rocchi et al. (2004)	0	0	0	700	33	Brittle	Etna "crust" basalt; strain rate = 10^{-5} s^{-1}
Rocchi et al. (2004)	0	0	0	800	42	Brittle	Vesuvius basalt; φ = 0.08–0.10; strain rate = 10^{-5} s^{-1}
Rocchi et al. (2004)	0	0	0	800	43	Brittle	Etna "core" basalt; strain rate = 10^{-4} s^{-1}
Rocchi et al. (2004)	0	0	0	800	25	Brittle	Etna "core" basalt; strain rate = 10^{-5} s^{-1}
Rocchi et al. (2004)	0	0	0	800	17	Brittle	Etna "core" basalt; strain rate = 10^{-6} s^{-1}
Rocchi et al. (2004)	0	0	0	800	20	Brittle	Etna "crust" basalt; strain rate = 10^{-4} s^{-1}
Rocchi et al. (2004)	0	0	0	900	50	Brittle	Vesuvius basalt; φ = 0.08–0.10; strain rate = 10^{-4} s^{-1}
Rocchi et al. (2004)	0	0	0	900	38	Brittle	Vesuvius basalt; φ = 0.08–0.10; strain rate = 10^{-5} s^{-1}
Rocchi et al. (2004)	0	0	0	900	29	Brittle	Vesuvius basalt; φ = 0.08–0.10; strain rate = 10^{-5} s^{-1}
Rocchi et al. (2004)	0	0	0	900	31	Brittle	Vesuvius basalt; φ = 0.08–0.10; strain rate = 10^{-6} s^{-1}
Rocchi et al. (2004)	5	0	5	25	108	Brittle	Vesuvius basalt; φ = 0.08–0.10; strain rate = 10^{-5} s^{-1}
Rocchi et al. (2004)	10	0	10	25	104	Brittle	Vesuvius basalt; φ = 0.08–0.10; strain rate = 10^{-5} s^{-1}
Rocchi et al. (2004)	10	0	10	300	101	Brittle	Vesuvius basalt; φ = 0.08–0.10; strain rate = 10^{-5} s^{-1}
Rocchi et al. (2004)	10	0	10	300	88	Brittle	Vesuvius basalt; φ = 0.08–0.10; strain rate = 10^{-5} s^{-1}
Rocchi et al. (2004)	10	0	10	600	116	Brittle	Vesuvius basalt; φ = 0.08–0.10; strain rate = 10^{-5} s^{-1}
Rocchi et al. (2004)	10	0	10	916	62	Brittle	Vesuvius basalt; φ = 0.08–0.10; strain rate = 10^{-5} s^{-1}
Rocchi et al. (2004)	12	0	12	25	93	Brittle	Vesuvius basalt; φ = 0.08–0.10; strain rate = 10^{-5} s^{-1}
Rocchi et al. (2004)	15	0	15	25	101	Brittle	Vesuvius basalt; φ = 0.08–0.10; strain rate = 10^{-5} s^{-1}
Rocchi et al. (2004)	17	0	17	25	100	Brittle	Vesuvius basalt; φ = 0.08–0.10; strain rate = 10^{-5} s^{-1}
Rocchi et al. (2004)	20	0	20	25	109	Brittle	Vesuvius basalt; φ = 0.08–0.10; strain rate = 10^{-5} s^{-1}
Rocchi et al. (2004)	20	0	20	300	95	Brittle	Vesuvius basalt; φ = 0.08–0.10; strain rate = 10^{-5} s^{-1}
Rocchi et al. (2004)	20	0	20	300	91	Brittle	Vesuvius basalt; φ = 0.08–0.10; strain rate = 10^{-5} s^{-1}
Rocchi et al. (2004)	20	0	20	600	118	Brittle	Vesuvius basalt; φ = 0.08–0.10; strain rate = 10^{-5} s^{-1}
Rocchi et al. (2004)	30	0	30	25	112	Brittle	Vesuvius basalt; φ = 0.08–0.10; strain rate = 10^{-5} s^{-1}
Rocchi et al. (2004)	30	0	30	25	103	Brittle	Vesuvius basalt; φ = 0.08–0.10; strain rate = 10^{-5} s^{-1}
Rocchi et al. (2004)	30	0	30	300	105	Brittle	Vesuvius basalt; φ = 0.08–0.10; strain rate = 10^{-5} s^{-1}
Rocchi et al. (2004)	30	0	30	300	87	Brittle	Vesuvius basalt; φ = 0.08–0.10; strain rate = 10^{-5} s^{-1}
Rocchi et al. (2004)	30	0	30	600	104	Brittle	Vesuvius basalt; φ = 0.08–0.10; strain rate = 10^{-5} s^{-1}
Rocchi et al. (2004)	30	0	30	604	79	Brittle	Vesuvius basalt; φ = 0.08–0.10; strain rate = 10^{-5} s^{-1}
Rocchi et al. (2004)	0	0	0	900	–	Ductile	Etna "crust" basalt; strain rate = 10^{-5} s^{-1}
Rocchi et al. (2004)	0	0	0	912	–	Ductile	Etna "core" basalt; strain rate = 10^{-5} s^{-1}
Rocchi et al. (2004)	0	0	0	1001	–	Ductile	Vesuvius basalt; φ = 0.08–0.10; strain rate = 10^{-5} s^{-1}
Apuani et al. (2005)	4	0	4	25	98	Brittle	Vigna Vecchia basalt (Stromboli)
Apuani et al. (2005)	4	0	4	25	72	Brittle	Vigna Vecchia basalt (Stromboli)
Apuani et al. (2005)	4	0	4	25	67	Brittle	Vigna Vecchia basalt (Stromboli)
Apuani et al. (2005)	8	0	8	25	88	Brittle	Vigna Vecchia basalt (Stromboli)
Apuani et al. (2005)	8	0	8	25	99	Brittle	Vigna Vecchia basalt (Stromboli)
Apuani et al. (2005)	12	0	12	25	104	Brittle	Vigna Vecchia basalt (Stromboli)
Apuani et al. (2005)	12	0	12	25	109	Brittle	Vigna Vecchia basalt (Stromboli)
Apuani et al. (2005)	16	0	16	25	54	Brittle	Vigna Vecchia basalt (Stromboli)
Apuani et al. (2005)	16	0	16	25	62	Brittle	Vigna Vecchia basalt (Stromboli)
Apuani et al. (2005)	16	0	16	25	87	Brittle	Vigna Vecchia basalt (Stromboli)
Apuani et al. (2005)	16	0	16	25	94	Brittle	Vigna Vecchia basalt (Stromboli)
Apuani et al. (2005)	20	0	20	25	56	Brittle	Vigna Vecchia basalt (Stromboli)
Apuani et al. (2005)	20	0	20	25	109	Brittle	Vigna Vecchia basalt (Stromboli)
Apuani et al. (2005)	20	0	20	25	178	Brittle	Vigna Vecchia basalt (Stromboli)
Benson et al. (2007)	60	20	40	25	475	Brittle	Etna basalt; φ = 0.04; strain rate = 10^{-6} s^{-1}
Ougier-Simonin et al. (2011)	15	0	15	25	370	Brittle	Seljadur basalt; φ = 0.05; strain rate = 10^{-6} s^{-1}
Heap et al. (2011)	30	20	10	25	291	Brittle	Etna basalt; φ = 0.4; strain rate = 10^{-5} s^{-1}
Heap et al. (2011)	50	20	30	25	287	Brittle	Etna basalt; φ = 0.4; strain rate = 10^{-5} s^{-1}
Heap et al. (2011)	70	20	50	25	504	Brittle	Etna basalt; φ = 0.4; strain rate = 10^{-5} s^{-1}
Heap et al. (2011)	50	20	30	25	375	Brittle	Etna basalt; φ = 0.4; creep test; strain rate = 10^{-6} s^{-1}
Heap et al. (2011)	50	20	30	25	357	Brittle	Etna basalt; φ = 0.4; creep test; strain rate = 10^{-7} s^{-1}
Heap et al. (2011)	50	20	30	25	329	Brittle	Etna basalt; φ = 0.4; creep test; strain rate = 10^{-8} s^{-1}
Heap et al. (2011)	50	20	30	25	304	Brittle	Etna basalt; φ = 0.4; creep test; strain rate = 10^{-9} s^{-1}
Violay et al. (2012)	100	0	100	400	1002	Brittle	Aphanitic basalt; φ = 0.02; strain rate = 10^{-5} s^{-1}
Violay et al. (2012)	100	0	100	400	902	Brittle	Porphyritic basalt; partially glassy; φ = 0.02; strain rate = 10^{-5} s^{-1}
Violay et al. (2012)	100	0	100	600	854	Brittle	Aphanitic basalt; φ = 0.02; strain rate = 10^{-5} s^{-1}
Violay et al. (2012)	100	0	100	700	508	Brittle	Aphanitic basalt; φ = 0.02; strain rate = 10^{-5} s^{-1}
Violay et al. (2012)	100	0	100	800	462	Brittle	Aphanitic basalt; φ = 0.02; strain rate = 10^{-5} s^{-1}
Violay et al. (2012)	100	0	100	800	446	Brittle	Aphanitic basalt; φ = 0.02; strain rate = 10^{-5} s^{-1}

(*continued on next page*)

Table 1 (*continued*)

Reference	*Pc* (MPa)	*Pp* (MPa)	*Peff* (MPa)	*T* (°C)	σ_p (MPa)	Failure mode	Notes
Violay et al. (2012)	100	0	100	900	355	Brittle	Aphanitic basalt; $\varphi = 0.02$; strain rate $= 10^{-5}$ s^{-1}
Violay et al. (2012)	300	0	300	600	749	Brittle	Aphanitic basalt; $\varphi = 0.02$; strain rate $= 10^{-5}$ s^{-1}
Violay et al. (2012)	300	0	300	700	755	Brittle	Aphanitic basalt; $\varphi = 0.02$; strain rate $= 10^{-5}$ s^{-1}
Violay et al. (2012)	300	0	300	800	518	Brittle	Aphanitic basalt; $\varphi = 0.02$; strain rate $= 10^{-5}$ s^{-1}
Violay et al. (2012)	50	0	50	600	–	Ductile	Porphyritic basalt; partially glassy; $\varphi = 0.02$; strain rate $= 10^{-5}$ s^{-1}
Violay et al. (2012)	70	0	70	600	–	Ductile	Porphyritic basalt; partially glassy; $\varphi = 0.02$; strain rate $= 10^{-5}$ s^{-1}
Violay et al. 2012	100	0	100	500	–	Ductile	Porphyritic basalt; partially glassy; $\varphi = 0.02$; strain rate $= 10^{-5}$ s^{-1}
Violay et al. 2012	100	0	100	600	–	Ductile	Porphyritic basalt; partially glassy; $\varphi = 0.02$; strain rate $= 10^{-5}$ s^{-1}
Violay et al. (2012)	100	0	100	600	–	Ductile	Porphyritic basalt; partially glassy; $\varphi = 0.02$; strain rate $= 10^{-5}$ s^{-1}
Violay et al. (2012)	100	0	100	700	–	Ductile	Porphyritic basalt; partially glassy; $\varphi = 0.02$; strain rate $= 10^{-5}$ s^{-1}
Violay et al. (2012)	100	0	100	800	–	Ductile	Porphyritic basalt; partially glassy; $\varphi = 0.02$; strain rate $= 10^{-5}$ s^{-1}
Violay et al. (2012)	100	0	100	800	–	Ductile	Porphyritic basalt; partially glassy; $\varphi = 0.02$; strain rate $= 10^{-5}$ s^{-1}
Violay et al. (2012)	100	0	100	800	–	Ductile	Porphyritic basalt; partially glassy; $\varphi = 0.02$; strain rate $= 10^{-5}$ s^{-1}
Violay et al. (2012)	100	0	100	900	–	Ductile	Porphyritic basalt; partially glassy; $\varphi = 0.02$; strain rate $= 10^{-5}$ s^{-1}
Violay et al. (2012)	100	0	100	900	–	Ductile	Porphyritic basalt; partially glassy; $\varphi = 0.02$; strain rate $= 10^{-5}$ s^{-1}
Violay et al. (2012)	100	0	100	900	–	Ductile	Porphyritic basalt; partially glassy; $\varphi = 0.02$; strain rate $= 10^{-5}$ s^{-1}
Violay et al. (2012)	250	0	250	650	–	Ductile	Porphyritic basalt; partially glassy; $\varphi = 0.02$; strain rate $= 10^{-5}$ s^{-1}
Violay et al. (2012)	300	0	300	600	–	Ductile	Porphyritic basalt; partially glassy; $\varphi = 0.02$; strain rate $= 10^{-5}$ s^{-1}
Violay et al. (2012)	300	0	300	700	–	Ductile	Porphyritic basalt; partially glassy; $\varphi = 0.02$; strain rate $= 10^{-5}$ s^{-1}
Violay et al. (2012)	300	0	300	750	–	Ductile	Porphyritic basalt; partially glassy; $\varphi = 0.02$; strain rate $= 10^{-5}$ s^{-1}
Violay et al. (2012)	300	0	300	800	–	Ductile	Porphyritic basalt; partially glassy; $\varphi = 0.02$; strain rate $= 10^{-5}$ s^{-1}
Violay et al. (2012)	300	0	300	800	–	Ductile	Aphanitic basalt; $\varphi = 0.02$; strain rate $= 10^{-5}$ s^{-1}
Violay et al. (2012)	300	0	300	850	–	Ductile	Aphanitic basalt; $\varphi = 0.02$; strain rate $= 10^{-5}$ s^{-1}
Violay et al. (2012)	300	0	300	900	–	Ductile	Aphanitic basalt; $\varphi = 0.02$; strain rate $= 10^{-5}$ s^{-1}
Violay et al. (2012)	300	0	300	900	–	Ductile	Porphyritic basalt; partially glassy; $\varphi = 0.02$; strain rate $= 10^{-5}$ s^{-1}
Benson et al. (2012)	0	0	0	200	143	Brittle	Etna basalt; $\varphi = 0.04$
Benson et al. (2012)	0	0	0	500	156	Brittle	Etna basalt; $\varphi = 0.04$
Benson et al. (2012)	0	0	0	750	153	Brittle	Etna basalt; $\varphi = 0.04$
Benson et al. (2012)	0	0	0	900	156	Brittle	Etna basalt; $\varphi = 0.04$
Benson et al. (2012)	0	0	0	950	187	Brittle	Etna basalt; $\varphi = 0.04$
Violay et al. (2012)	300	0	300	950	–	Ductile	Aphanitic basalt; $\varphi = 0.02$; strain rate $= 10^{-5}$ s^{-1}
Adelinet et al. (2013)	10	5	5	25	120	Brittle	Reykjanes basalt; $\varphi = 0.08$; strain rate $= 10^{-6}$ s^{-1}
Adelinet et al. (2013)	80	76	4	25	118	Brittle	Reykjanes basalt; $\varphi = 0.08$; strain rate $= 10^{-6}$ s^{-1}
Violay et al. (2015)	130	30	100	600	877	Brittle	Aphanitic basalt; $\varphi = 0.03$; strain rate $= 10^{-5}$ s^{-1}
Violay et al. (2015)	130	30	100	650	834	Brittle	Aphanitic basalt; $\varphi = 0.03$; strain rate $= 10^{-5}$ s^{-1}
Violay et al. (2015)	130	30	100	700	792	Brittle	Aphanitic basalt; $\varphi = 0.03$; strain rate $= 10^{-5}$ s^{-1}
Violay et al. (2015)	130	30	100	750	699	Brittle	Aphanitic basalt; $\varphi = 0.03$; strain rate $= 10^{-5}$ s^{-1}
Violay et al. (2015)	130	30	100	800	717	Brittle	Aphanitic basalt; $\varphi = 0.03$; strain rate $= 10^{-5}$ s^{-1}
Violay et al. (2015)	130	30	100	900	382	Brittle	Aphanitic basalt; $\varphi = 0.03$; strain rate $= 10^{-5}$ s^{-1}
Violay et al. (2015)	130	30	100	1050	–	Ductile	Aphanitic basalt; $\varphi = 0.03$; strain rate $= 10^{-5}$ s^{-1}
Schaefer et al. (2015)	0	0	0	935	167	Brittle	Pacaya (Guatemala) basalt; $\varphi = 0.02$; strain rate $= 10^{-1}$ s^{-1}
Schaefer et al. (2015)	0	0	0	935	162	Brittle	Pacaya (Guatemala) basalt; $\varphi = 0.05$; strain rate $= 10^{-1}$ s^{-1}
Schaefer et al. (2015)	0	0	0	935	126	Brittle	Pacaya (Guatemala) basalt; $\varphi = 0.06$; strain rate $= 10^{-5}$ s^{-1}
Schaefer et al. (2015)	0	0	0	935	59	Brittle	Pacaya (Guatemala) basalt; $\varphi = 0.19$; strain rate $= 10^{-1}$ s^{-1}
Schaefer et al. (2015)	0	0	0	935	49	Brittle	Pacaya (Guatemala) basalt; $\varphi = 0.16$; strain rate $= 10^{-5}$ s^{-1}
Schaefer et al. (2015)	0	0	0	935	93	Brittle	Pacaya (Guatemala) basalt; $\varphi = 0.19$; strain rate $= 10^{-1}$ s^{-1}
Schaefer et al. (2015)	0	0	0	935	44	Brittle	Pacaya (Guatemala) basalt; $\varphi = 0.19$; strain rate $= 10^{-5}$ s^{-1}
Schaefer et al. (2015)	0	0	0	935	75	Brittle	Pacaya (Guatemala) basalt; $\varphi = 0.23$; strain rate $= 10^{-1}$ s^{-1}

(*continued on next page*)

Table 1 (*continued*)

Reference	*Pc* (MPa)	*Pp* (MPa)	*Peff* (MPa)	*T* (°C)	σ_p (MPa)	Failure mode	Notes
Schaefer et al. (2015)	0	0	0	935	64	Brittle	Pacaya (Guatemala) basalt; $\varphi = 0.21$; strain rate = 10^{-5} s^{-1}
Schaefer et al. (2015)	0	0	0	935	28	Brittle	Pacaya (Guatemala) basalt; $\varphi = 0.32$; strain rate = 10^{-1} s^{-1}
Schaefer et al. (2015)	0	0	0	935	16	Brittle	Pacaya (Guatemala) basalt; $\varphi = 0.31$; strain rate = 10^{-5} s^{-1}
Zhu et al. (2016)	20	10	10	25	281	Brittle	Etna basalt (EB_I); $\varphi = 0.05$; strain rate = 10^{-5} s^{-1}
Zhu et al. (2016)	20	10	10	25	240	Brittle	Etna basalt (EB_I); $\varphi = 0.05$; strain rate = 10^{-5} s^{-1}
Zhu et al. (2016)	20	10	10	25	221	Brittle	Etna basalt (EB_I); $\varphi = 0.05$; strain rate = 10^{-5} s^{-1}
Zhu et al. (2016)	20	10	10	25	327	Brittle	Etna basalt (EB_I); $\varphi = 0.05$; strain rate = 10^{-5} s^{-1}
Zhu et al. (2016)	30	10	20	25	329	Brittle	Etna basalt (EB_I); $\varphi = 0.05$; strain rate = 10^{-5} s^{-1}
Zhu et al. (2016)	30	10	20	25	361	Brittle	Etna basalt (EB_I); $\varphi = 0.05$; strain rate = 10^{-5} s^{-1}
Zhu et al. (2016)	40	10	30	25	399	Brittle	Etna basalt (EB_I); $\varphi = 0.05$; strain rate = 10^{-5} s^{-1}
Zhu et al. (2016)	50	10	40	25	403	Brittle	Etna basalt (EB_I); $\varphi = 0.05$; strain rate = 10^{-5} s^{-1}
Zhu et al. (2016)	60	10	50	25	500	Brittle	Etna basalt (EB_I); $\varphi = 0.05$; strain rate = 10^{-5} s^{-1}
Zhu et al. (2016)	60	10	50	25	493	Brittle	Etna basalt (EB_I); $\varphi = 0.05$; strain rate = 10^{-5} s^{-1}
Zhu et al. (2016)	60	10	50	25	561	Brittle	Etna basalt (EB_I); $\varphi = 0.05$; strain rate = 10^{-5} s^{-1}
Zhu et al. (2016)	80	10	70	25	563	Brittle	Etna basalt (EB_I); $\varphi = 0.05$; strain rate = 10^{-5} s^{-1}
Zhu et al. (2016)	90	10	80	25	560	Brittle	Etna basalt (EB_I); $\varphi = 0.05$; strain rate = 10^{-5} s^{-1}
Zhu et al. (2016)	90	10	80	25	574	Brittle	Etna basalt (EB_I); $\varphi = 0.05$; strain rate = 10^{-5} s^{-1}
Zhu et al. (2016)	90	10	80	25	655	Brittle	Etna basalt (EB_I); $\varphi = 0.05$; strain rate = 10^{-5} s^{-1}
Zhu et al. (2016)	110	10	100	25	658	Brittle	Etna basalt (EB_I); $\varphi = 0.04$; strain rate = 10^{-5} s^{-1}
Zhu et al. (2016)	160	10	150	25	753	Brittle	Etna basalt (EB_I); $\varphi = 0.05$; strain rate = 10^{-5} s^{-1}
Zhu et al. (2016)	60	10	50	25	365	Brittle	Etna basalt (EB_II); $\varphi = 0.08$; strain rate = 10^{-5} s^{-1}
Zhu et al. (2016)	90	10	80	25	349	Brittle	Etna basalt (EB_II); $\varphi = 0.08$; strain rate = 10^{-5} s^{-1}
Zhu et al. (2016)	20	10	10	25	224	Brittle	Etna basalt (EB_III); $\varphi = 0.05$; strain rate = 10^{-5} s^{-1}
Zhu et al. (2016)	60	10	50	25	434	Brittle	Etna basalt (EB_III); $\varphi = 0.05$; strain rate = 10^{-5} s^{-1}
Zhu et al. (2016)	90	10	80	25	543	Brittle	Etna basalt (EB_III); $\varphi = 0.05$; strain rate = 10^{-5} s^{-1}
Zhu et al. (2016)	110	10	100	25	640	Brittle	Etna basalt (EB_III); $\varphi = 0.05$; strain rate = 10^{-5} s^{-1}
Zhu et al. (2016)	160	10	150	25	798	Brittle	Etna basalt (EB_III); $\varphi = 0.05$; strain rate = 10^{-5} s^{-1}

elevated-temperature experiments were deformed inside a tube furnace. Most of the experiments were performed on nominally dry samples, but some samples were saturated with a fluid phase (distilled water or argon gas) and thus were subject to a pore fluid pressure. We consider here a simple effective pressure law where the effective pressure *Peff* is equal to the confining pressure *Pc* minus the pore pressure *Pp*, and we adopt the convention that compressive stresses and strains are positive.

We classified the failure mode of the deformed experimental samples as either brittle (i.e., the mechanical data show a large stress drop and/or the sample displayed a throughgoing fracture) or ductile (i.e., no large stress drop in the mechanical data and/or no evidence of strain localisation) (see Rutter, 1986). We use these definitions here to describe deformation on the sample lengthscale. Exemplary mechanical data showing typical brittle and ductile behaviour are shown in Fig. 1 (data from Violay et al., 2012). Of note, we have not considered here either instances of ductility as a result of microcracking or cataclastic pore collapse (Shimada, 1986; Shimada et al., 1989; Adelinet et al., 2013; Zhu et al., 2016) or experiments performed under uniaxial conditions and at room temperature (e.g., Al-Harthi et al., 1999; Heap et al., 2009).

Each experiment was performed at a constant effective pressure (Table 1). To plot a lithospheric failure mode map for Earth and Mars, we must convert this pressure to a depth. To perform this conversion, we determined pressure (lithostatic minus hydrostatic) gradients for Earth and Mars. The lithostatic and hydrostatic pressure gradients for Earth and Mars were calculated with $P = \rho g z$, where we assume a constant g = 9.807 and 3.711 m/s^2 for Earth and Mars, respectively. The hydrostatic pressure gradient was determined using a constant density ρ of 1000 kg/m^3 for both Earth and Mars (i.e., liquid water). This yields pore pressure gradients of ~10 and ~3.7 MPa/km for Earth and Mars, respectively. The density ρ of the Terran and Martian lithosphere, required for the calculation of their lithostatic pressure gradients, was determined using the following relation (Wilson and Head, 1994):

$$\rho(h) = \frac{\rho_\infty}{[1 + \{V_0 - (1 - V_0)\} \exp(-\lambda \rho_\infty g z)]}, \quad (1)$$

where ρ_∞ (the density of porosity-free rock) is taken as 2900 kg/m^3, V_0 is the void space fraction (i.e., total porosity) at the surface (assumed here to be 0.25; see Wilson and Head, 1994), and constant λ is assumed to be 1.18 × 10^{-8} Pa^{-1} (Head and Wilson, 1992). Eq. (1) predicts that the density of the lithosphere increases (or porosity decreases) at a greater rate as depth increases on Earth than on Mars (up to a maximum density of 2900 kg/m^3; Fig. 2).

The experimental data were plotted (indicating the failure mode) on graphs of temperature versus depth for Earth (Fig. 3a) and for Mars (Fig. 3b). The Terran thermal gradient was assumed to be 25 K/km (Fig. 3a). For Mars, we used a range of Martian thermal gradients, from 5 to 40 K/km (Fig. 3b), chosen to reflect the range of thermal gradients expected for Mars throughout its thermal evolution (Ruiz et al., 2011). The average surface temperature of Earth and Mars was taken as 288 K and 253 K, respectively. By following a particular thermal gradient on Fig. 3, one can estimate the depths at which brittle and ductile behaviour are encountered on Earth and Mars using the failure mode of adjacent experimental datapoints.

These data predict a switch from brittle to ductile behaviour at a depth of ~25 km for Earth (Fig. 3a), consistent with the broad (~10–40 km) depth predicted for basaltic oceanic lithosphere on Earth estimated with strength envelopes (Kohlstedt et al., 1995). The same data suggest that the transition from brittle to ductile behaviour on Mars would lie between 30–40 km for a thermal gradient of 25 K/km (Fig. 3b). Therefore, all else being equal, the BDT on Mars is deeper than on Earth solely as a function of surface gravity. The data suggest that the Martian lithosphere would remain brittle until the liquidus of basalt (Green and Ringwood, 1967) is reached at ~20–25 km for the highest thermal gradient of 40 K/km and an astonishing depth of > 100 km is pre-

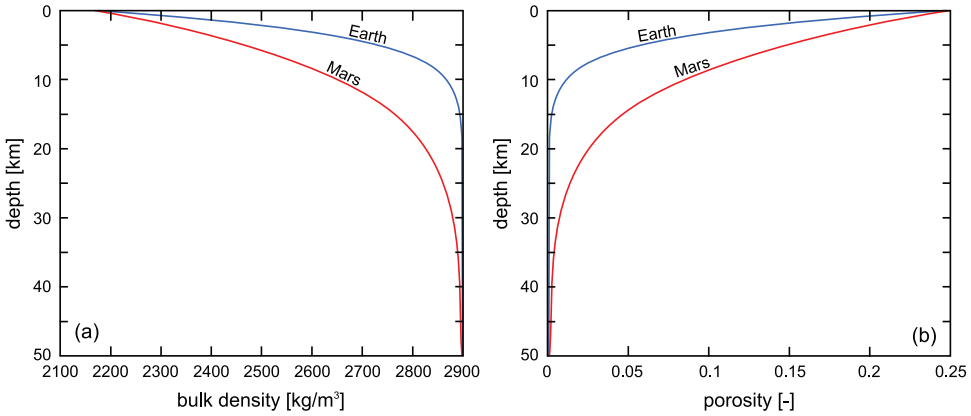

Fig. 2. The evolution of bulk density (a) and porosity (b) as a function of depth on Earth (blue curves) and Mars (red curves). Curves calculated using Eq. (1) (see also Wilson and Head, 1994). (For interpretation of the references to colour in this figure legend, the reader is referred to the web version of this article.)

dicted for the BDT when the thermal gradient is as low as 5 K/km (Fig. 3b). Our analysis therefore provides an additional technique to characterise how the Martian lithosphere thickened as Mars cooled over time (see also Baratoux et al., 2011).

The inversion of present-day tectonic features, corresponding to the final state of lithospheric deformation in response to vertical loading, has been used to provide estimations for the depth of the BDT on Mars (Solomon and Head, 1990; Schultz and Watters, 2001; Montési and Zuber, 2003; Wilkins and Schultz, 2003; Grott et al., 2007; Ruiz et al., 2008). The BDT is defined in these studies as the depth to a temperature at which ductile behaviour replaces brittle behaviour, and is taken to be equal to the thickness of the elastic lithosphere. Solomon and Head (1990) reported BDT values of 18–26 km beneath Arsia, Ascraeus, and Pavonis Montes, 54 km under Elysium Mons, 110–230 km for beneath Olympus Mons, and depths greater than 100 km for the Isidis mascon and the Tharsis rise. Additional estimates of the Martian BDT have been reported as 25–35 km for Amenthes Rupes (Schultz and Watters, 2001; Ruiz et al., 2008), 21–35 km beneath the southern Thaumasia region (Grott et al., 2007), 30–50 km under Solis and Lunae Plana (Montési and Zuber, 2003), and 60–100 km for the northern lowlands (Montési and Zuber, 2003). Additionally, penetration depths of between 60 and 75 km have been estimated for normal faults within Valles Marineris (Wilkins and Schultz, 2003). The calculated thermal gradients corresponding to the BDT depths derived by these studies are in agreement with those we find through our approach (Fig. 3b). For instance, for a thermal gradient of 10 K/km, the data show that the BDT on Mars is ~70 km (Fig. 3b). This prediction is consistent with BDT and calculated thermal gradient for Elysium Mons (BDT = 48–110 km; thermal gradient = 6–14 K/km; Solomon and Head, 1990 and references therein). The data and experimental approach adopted here could therefore act as an independent and useful method with which to estimate thermal gradients and the depth of the BDT on a planetary body with a basaltic (or mechanically cognate) primary crustal lithology (including the Moon, Mars, Venus, and telluric super-Earths).

However, thermal gradients calculated with estimates of the BDT from tectonic features on the surface of Mars likely underestimate the Martian thermal gradient during the Noachian and early Hesperian when the Tharsis Montes and Olympus Mons were volcanically active (Hauck and Phillips, 2002; Ruiz et al., 2011; Ruiz, 2014). We also note that hydrothermal alteration during the Noachian would have required a thermal gradient in excess of 20 K/km (McSween et al., 2015). We include a (perhaps unrealistically) high thermal gradient of 40 K/km for this reason (Fig. 3b). The data suggest that brittle behaviour would persist to a depth of ~20–25 km (i.e., similar to that estimated for present-day Earth; Fig. 3a) on Mars even if the thermal gradient was as high as 40 K/km (Fig. 3b).

The data shown in Fig. 3 assume a hydrostatic pore pressure. However, large channels within areas of chaotic terrain on Mars are thought to be the consequence of erosion by water released from high-pressure aquifers (Carr, 1979). The surface of Mars is replete with examples of large erosional valleys and channels and, although most of these features were formed during the Hesperian, there are examples of more recent Amazonian channels (Carr and Head, 2010 and references therein). As a result, pore fluid pressures in the Martian lithosphere may have exceeded hydrostatic pore pressure for a large portion of its geological history. We therefore provide an additional failure mode map for Mars assuming a pore pressure twice that of the hydrostatic (~7.4 MPa/km) (Fig. 4). A higher pore pressure increases the depth of the BDT for thermal gradients between 5 and 15 K/km (Fig. 4). For example, the BDT increases in depth from ~70 to ~80 km when the thermal gradient is 10 K/km. However, the depth of the BDT remains largely unchanged for higher thermal gradients (25–40 K/km). When the thermal gradient is 40 K/km, for example, brittle behaviour is still expected until the liquidus of basalt is reached at ~20–25 km (Fig. 4).

To conclude, an analysis of experimental rock deformation data (Figs. 3 and 4; Table 1) suggests that the brittle lithosphere can be much thicker on Mars than on Earth as a result of surface gravity alone. To emphasise this point, our analysis shows that the depth of BDT on Mars can be deeper even when the thermal gradient is about twice that of present-day Earth (Figs. 3 and 4). However, more experimental data, particularly at low temperatures and high pressures, are now required to develop such predictions.

2.2. Influence of surface gravity on the strength (resistance to failure) of the brittle lithosphere

An increase in lithostatic pressure reduces the ease with which fractures can nucleate and propagate (Jaeger et al., 2007). As a result, the brittle strength of rock increases as lithostatic pressure increases (Paterson and Wong, 2005). Here, we once again utilise published experimental data (acquired under various pressures and temperatures) for the compressive strength of basalts in the brittle field (Table 1) to derive strength profiles for the Terran and Martian lithospheres. As before, we excluded some published data from our analysis: in this case only experiments performed under uniaxial conditions. The experimental effective pressures were converted to depths as described above.

We provide here lithospheric strength profiles for the hydrostatic case (Fig. 5a) and, as above, a scenario for which the Martian

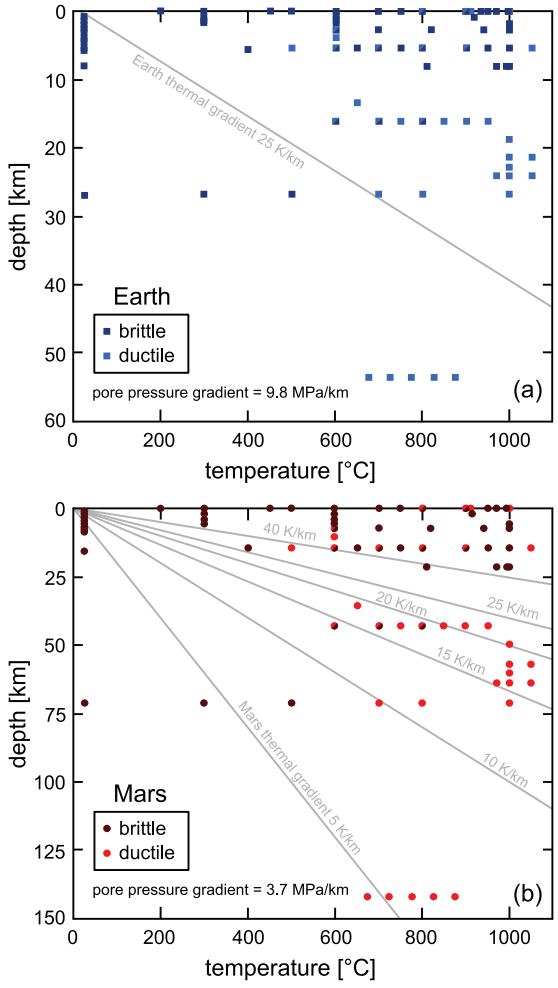

Fig. 3. Depth of the brittle–ductile transition (BDT) for hydrostatic conditions. Depth against temperature for Earth (a) and Mars (b) populated with experimental data from triaxial deformation experiments on basalt (and diabase) performed at different pressure and temperature conditions (Table 1). These experiments were classed as either brittle or ductile (see Fig. 1 for details of failure mode classification). The Terran geotherm (25 K/km) and a range of Martian thermal gradients (from 5 to 40 K/km) are shown on panels (a) and (b), respectively.

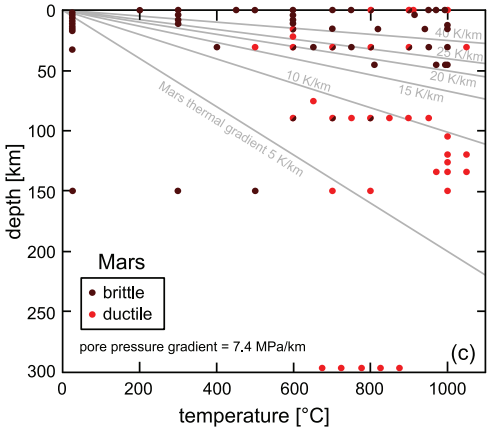

Fig. 4. Depth of the brittle–ductile transition (BDT) on Mars assuming a pore pressure gradient twice that of the hydrostatic. As per Fig. 3, the experimental data (Table 1) are plotted on a graph of depth against temperature and a range of Martian thermal gradients are provided (from 5 to 40 K/km).

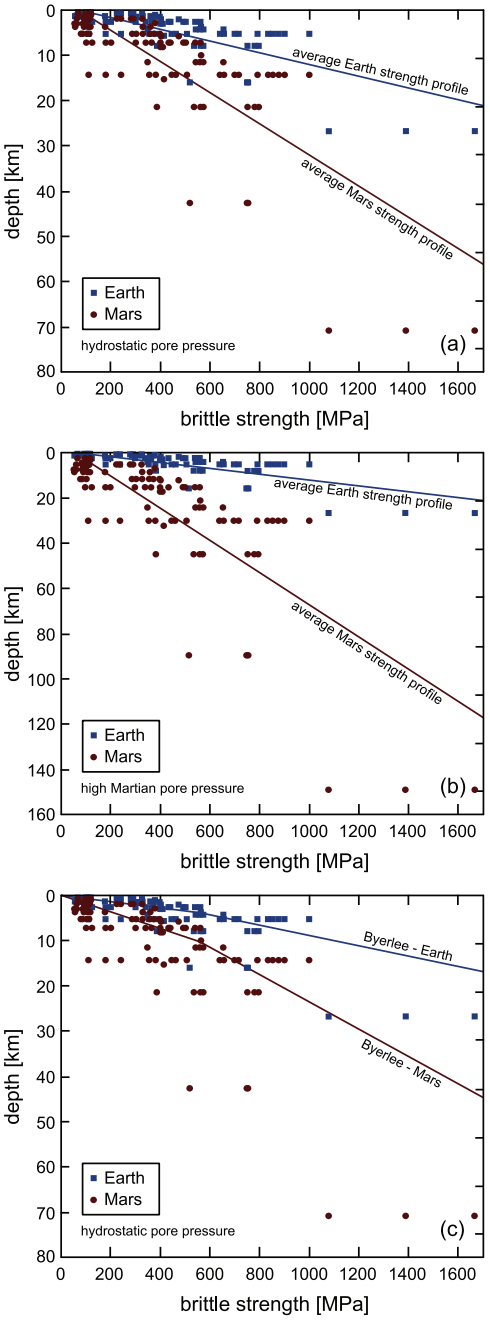

Fig. 5. Brittle lithosphere strength profiles. (a) Depth against brittle strength for Earth (blue squares) and Mars (red circles) assuming hydrostatic conditions. (b) Depth against brittle strength for Earth (blue squares) and Mars (red circles) assuming that the pore pressure on Mars is twice that of the hydrostatic. Experimental data were taken from triaxial deformation experiments performed on basalt (and diabase) at different pressure and temperature conditions (Table 1). Average strength profiles for Earth and Mars are simply linear fits to the experimental data. (c) Depth against brittle strength for Earth (blue squares) and Mars (red circles) assuming hydrostatic conditions (the same plot as in panel a), together with the lithospheric strength profiles predicted using Byerlee's rule (Eq. (2); see text for details). (For interpretation of the references to colour in this figure legend, the reader is referred to the web version of this article.)

pore pressure gradient is twice that of the hydrostatic (Fig. 5b). A limitation of this approach is that brittle strength is both time- and scale-dependent. Strength in the brittle field is known to exhibit a time-dependency due to subcritical crack growth (Brantut et al., 2013). Since the majority of the compiled experiments were performed at strain rates that greatly exceed real-world strain rates

(Table 1), the strengths provided here are likely overestimated. For example, the strength of basalt was reduced from 375 to 304 MPa when the strain rate was reduced from 10^{-6} to 10^{-9} s^{-1} (Heap et al., 2011). Brittle strength is also scale-dependent (Schultz, 1993; 1995) and therefore the strength values for initially intact rock likely overestimate the strength of a rock mass (i.e., at fracture lengthscales greater than the macrofracture spacing). Estimates of rock mass strength can be provided using fracture criteria such as the Hoek–Brown criterion (Hoek and Brown, 1980) that ultilise rock mass classification schemes such as the Rock Mass Rating system (RMR) (Bieniawski, 1989) or the Geological Strength Index (GSI) (Hoek, 1994). These techniques have been previously employed to offer insight into the stability of rock slopes (Neuffer and Schultz, 2006; Okubo et al., 2011), plantery contraction (Klimczak, 2015), and planetary ring formation (Black and Mittal, 2015). However, such criteria require an estimation of the degree of fracturing (using, for example, the RMR or GSI classification scheme) and the selection of a representative basalt. Owing to the difficulty in selecting a basalt that best represents the Terran and Martian lithospheres (where strength depends very much on the physical attributes of the basalt, which could vary considerably), we choose here to show the intact strength for all of the compiled data to simply understand whether (and to what degree) the Martian lithosphere is weaker than the Terran lithosphere at a given depth as a function of surface gravity alone. We emphasise that rock mass strength analysis would reduce the Terran and Martian strength profiles equally, thereby maintaining the lithospheric strength discrepancy, or exacerbate the difference if the Martian lithosphere is more fractured. GSI estimates for the Martian lithosphere have been found to be similar to rock masses on Earth (Klimczak, 2015).

The data show that, for a given depth, the strength of the Martian lithosphere is considerably lower than that of Earth (Fig. 5a and b). Although there is scatter in these data (due to variations in experimental temperature and rock attributes including porosity and pore size, amongst others; Table 1), a line of best fit indicates that, at a depth of 10 km, the difference in compressive strength of the Terran and Martian lithosphere is substantial when the pore pressure is hydrostatic (~900 and ~350 MPa, respectively; Fig. 5a). This strength discrepancy becomes greater when we assume a Martian pore pressure gradient twice that of the hydrostatic (Fig. 5b). In this scenario, brittle strength at 10 km depth on Mars is reduced from ~350 to ~200 MPa (Fig. 5). An interrogation of experimental rock deformation data (Fig. 5a and b) therefore suggests that the brittle lithosphere is much weaker on Mars than on Earth for a given depth due to surface gravity alone.

If we assume a constant bulk density for the Terran and Martian lithospheres of 2900 kg/m^3, we can compare these intact compressive strength data with those predicted for sliding on a pre-existing discontinuity using Byerlee's rule (Brace and Kohlstedt, 1980; Kohlstedt and Mackwell, 2010; Klimczak, 2015):

$$\begin{aligned} \sigma_1 &\cong 5\sigma_3 \quad \text{for} \quad \sigma_3 < 110 \text{ MPa} \\ \sigma_1 &\cong 3.1\sigma_3 + 210 \quad \text{for} \quad \sigma_3 > 110 \text{ MPa}, \end{aligned} \tag{2}$$

where σ_1 and σ_3 are the greatest and least principal stresses, respectively. We note that Byerlee's rule (Byerlee, 1978) is essentially independent of rock type. Although Byerlee's rule predicts unrealistic values for near-surface strength, values at depth do not depend on selecting a representative basalt, as would be the case for the Coulomb criterion for frictional sliding. The modelled curves are plotted alongside the intact compressive strength data for the hydrostatic case in Fig. 5c. Of interest, the lithospheric strength profiles predicted using Byerlee's rule follow similar trends to those found using the compiled intact strength data (Fig. 5c).

We note that the propagation of dykes—and thus the transport of magma—is more directly determined by the tensile strength of basalt, rather than their compressive strengths (shown here). However, laboratory tensile strength data for basalt are rare and, to our knowledge, only collected under ambient laboratory conditions (Schultz, 1993; 1995; Apuani et al., 2005). Since the tensile strength of a given rock type is typically about a twelfth of its compressive strength (Jaeger et al., 2007), we expect that the tensile strength of basalt will follow a similar trend to compressive strength profiles shown in Fig. 5.

2.3. Influence of surface gravity on the aperture of fractures within the brittle lithosphere

Beyond increasing the difficulty at which fractures can nucleate and propagate, a higher lithostatic pressure will serve to reduce the aperture of pre-existing extension fractures or joints (i.e., "opening-mode" or Mode I fractures). For example, the permeability of micro- and macrofractured basalt dramatically decreases as confining pressure (i.e., depth) increases (Vinciguerra et al., 2005; Nara et al., 2011). This reduction in permeability is the result of the closure of fractures, which are readily squeezed shut with increased confining or lithostatic pressure. The lower surface gravity of Mars will therefore allow fractures to remain open to greater depths than on Earth (thereby increasing the fracture density) and fractures to be wider at a given depth, on Mars than on Earth.

2.4. Influence of surface gravity on the maximum depth for downward-propagating extension fractures

Downward-propagating extension fractures or joints will resolve a shear component (i.e., the fractures will transition to normal faults) once the following relation has been satisfied (Mège and Masson, 1997; Gudmundsson, 2011):

$$d_{max} = \frac{3\sigma_t}{\rho g}, \tag{3}$$

where d_{max} is the maximum penetration depth, σ_t is the tensile strength of the rock, and ρ is the bulk rock density. If we assume a constant bulk density ($\rho = 2900$ kg/m^3) and tensile strength for basalt ($\sigma_t = 12$ MPa for intact basalt; Schultz et al., 1995), the difference in surface gravity on Mars ($g = 3.711$ m/s^2) and Earth ($g = 9.807$ m/s^2) results in a maximum propagation depth for extension fractures (i.e., joints) of ~3.3 and ~1.3 km, respectively. Using values estimated for the tensile strength of a fractured basaltic rock mass ($\sigma_t = 1$ MPa; Schultz et al., 1995), these propagation depths would be reduced to ~280 and ~100 m for Mars and Earth, respectively. Nevertheless, all else being equal, joints on Mars will penetrate farther into the lithosphere than those on Earth. However, although downward-propagating extensional fractures or joints can be deeper on Mars than on Earth, displacement–length scaling relations for faults (with normal and reverse senses of displacement) are consistently smaller, also interpreted as a consequence of the low surface gravity of Mars (Schultz et al., 2006).

3. Implications for martian volcanism, topography, and groundwater storage and circulation

We have shown here, with published experimental data (Table 1), that the lower surface gravity on Mars compared with Earth can serve to (1) increase the depth of the BDT, (2) reduce the strength of the brittle lithosphere at a given depth, (3) increase the porosity of the lithosphere, (4) increase the average fracture aperture at a given depth, (5) increase the depth at which fractures can remain open (and therefore fracture density), and (6) increase the maximum propagation depth for opening-mode fractures.

The differences between Martian and Terran volcanism (Carr, 1973; Greely and Spudis, 1981; Wilson and Head, 1983, 1994; Wilson, 2009) have been attributed at least in part to the lower surface gravity on Mars (Wilson and Head, 1994). Amongst other contributing factors, the lower surface gravity of Mars is expected to result in (1) a lower density for buried rock at a given depth, thus increasing the depth at of the neutral buoyancy zone (i.e., the depth at which magma stalls and coalesces as magma chambers), (2) a greater depth for gas nucleation and fragmentation for volatile-bearing magmas, and (3) a greater run-out distance for cooling-limited lava flows (Wilson and Head, 1994 and references therein). However, the influence of the lower Martian surface gravity on the mechanical behaviour of its lithosphere has received sparse attention. For example, the ease of dyke propagation—the principal mode of magma transport in the lithosphere (Rubin, 1995; Gudmundsson, 2006)—is likely enhanced by the weak Martian brittle lithosphere relative to Earth (Fig. 5). Further, the Martian lithosphere can host wider dykes than on Earth for a given depth (see also Wilson and Head, 1994 and references therein). Although these factors are likely to assist surface magma delivery, magma on Mars may have to travel farther due to the increased depth of the neutral buoyancy zone (itself a function of surface gravity; Wilson and Head, 1994) and many dykes may arrest before reaching the surface (Gudmundsson, 2002). Indeed, there is evidence to suggest that a large proportion of dykes within the Tharsis and Syrtis regions of Mars never broke the surface (Lillis et al., 2009; Black and Manga, 2016). Nevertheless, we expect that a weak Martian lithosphere that can host wide dykes greatly assisted magma delivery to the surface during volcanically active phases in the planet's past. We therefore contend that the lower surface gravity on Mars supports the high magma discharge rates inferred for the planet during the Noachian and early Hesperian (e.g., Cattermole, 1987; Wilson et al., 2001; Fuller and Head, 2003; Head et al., 2006; Hopper and Leverington, 2014), and thus the voluminous lava flows and enormous volcanoes observed on its surface (Greely and Spudis, 1981; Tanaka, 1986; Plescia, 1990; McEwen et al., 1999; Wilson and Head, 1994), relative to Earth. We further note that enhanced endogenous growth—intrusive–extrusive ratios predicted for the Tharsis and Syrtis regions are higher than most volcanic centres on Earth (Black and Manga, 2016)—could also help explain why volcanoes can be larger on Mars than on Earth, facilitated by a weak lithosphere/volcanic edifice (Fig. 5). The enormous height of the volcanoes of Mars are supported by the planet's thick, brittle lithosphere (Figs. 3 and 4): the ability of the lithosphere to support topographic loads without deflection increases as its rigidity (effectively its thickness) increases (Turcotte et al., 1981; Byrne et al., 2013). The support of tall structures provided by the thick Martian lithosphere may help explain the Martian topographic dichotomy (McGill and Squyres, 1991; Smith and Zuber, 1996; Watters et al., 2007).

Prolonged impact bombardment (MacKinnon and Tanaka, 1989; Rodriguez et al., 2005) and lithospheric loading (Solomon and Head, 1982; Zuber et al., 2000; Phillips et al., 2001) has left the Martian lithosphere substantially fractured. We suggest here that these fractures within the thick Martian lithosphere (Figs. 3 and 4) are abundant and pervasive, facilitated by the lithosphere's low strength (Fig. 5). The strength of the Martian crust may be further compromised by extensive weathering (Wyatt and McSween, 2002) and hydrothermal alteration (McSween et al., 2015), which is known to reduce the strength of rock (Pola et al., 2012; Wyering et al., 2014). Fractures at all scales will serve to increase the permeability of the lithosphere (Nara et al., 2011; Heap and Kennedy, 2016). Further, our analysis also suggests that fractures on Mars will be wider at a given depth than on Earth. The permeability of a fracture depends heavily on its aperture, eloquently demonstrated by the exact solution for a fracture containing smooth, parallel walls (Zimmerman and Bodvarsson, 1996):

$$k_f = \frac{h^2}{12}, \quad (4)$$

where k_f is the permeability of the fracture and h is the fracture aperture. It follows therefore that subsurface fluids will be more mobile through the lithosphere on Mars than on Earth. Note, aqueous fluids have been observed to have remained static within the Earth's lithosphere for almost 2 Ga (Holland et al., 2013). A highly permeable lithosphere will assist the crustal-scale movement of groundwater from the poles to the equator, inferred to play a key role in the geomorphic evolution and long-term cycling of H_2O between the Martian atmosphere, polar caps, and near-surface lithosphere (Clifford, 1993).

The storage capacity of the Martian lithosphere will also be greater relative to that of Earth's due to its greater thickness, a greater abundance of wide fractures, and the slower rate of porosity decrease as depth increases (Fig. 2; Wilson and Head, 1994). A high lithospheric storage capacity could help provide the high volumes invoked to explain, for example, catastrophic flooding events on Mars (Carr, 1979; MacKinnon and Tanaka, 1989; Baker et al., 1991; Baker, 2001; Plescia, 2003; Head et al., 2004; Rodriguez et al., 2005; Coleman et al., 2007; Warner et al., 2009). A porous and permeable lithosphere is also consistent with the notion that the absence of surface runoff following bolide impacts could be a function of ground infiltration and subsurface water sequestration, rather than a climate too cold for substantial precipitation (Carr, 2000).

And so it is that surface gravity, influenced by the mass of a given planetary body, can greatly modify the mechanical and hydraulic behaviour of its lithosphere, with attendant implications for its surface topography (Mars has the capacity to build and maintain enormous volcanoes, for example) and geomorphology, volcanic character, and groundwater storage and circulation. These inferences can be tested by data returned by the upcoming InSight mission to Mars (Banerdt et al., 2013), due to reach the Red Planet in 2018.

Acknowledgements

The first author acknowledges funding from an Initiative d'Excellence (IDEX) "Attractivité" grant (VOLPERM), funded by the University of Strasbourg. M.H. also acknowledges support from the CNRS (INSU 2016-TelluS-ALEAS). The idea for this paper was formulated during the International Venus Conference (Oxford, 2016), and we are therefore indebted to the conference organisers, and in particular to Colin Wilson. We acknowledge the constructive comments of two anonymous reviewers.

References

Adelinet, M., Fortin, J., Schubnel, A., Guéguen, Y., 2013. Deformation modes in an icelandic basalt: from brittle failure to localized deformation bands. J. Volcanol. Geotherm. Res. 255, 12–25.
Aharonson, O., Zuber, M.T., Rothman, D.H., 2001. Statistics of Mars' topography from the Mars Orbiter Laser Altimeter: Slopes, correlations, and physical models. J. Geophys. Res. 106, 23723–23735.
Al-Harthi, A.A., Al-Amri, R.M., Shehata, W.M., 1999. The porosity and engineering properties of vesicular basalt in saudi arabia. Eng. Geol. 54, 313–320.
Apuani, T., Corazzato, C., Cancelli, A., Tibaldi, A., 2005. Physical and mechanical properties of rock masses at Stromboli: a dataset for volcano instability evaluation. Bull. Eng. Geol. Environ. 64, 419–431.
Baker, V.R., Strom, R.G., Gulick, V.C., Kargel, J.S., Komatsu, G., Kale, V.S., 1991. Ancient oceans, ice sheets and the hydrological cycle on Mars. Nature 352, 589–594.
Baker, V.R., 2001. Water and the martian landscape. Nature 412, 228–236.
Banerdt, W.B., 29 co-authors, 2013. InSight: a discovery mission to explore the interior of Mars. Lunar and Planetary Science Conference, 44 abstract 1915.
Baratoux, D., Toplis, M.J., Monnereau, M., Gasnault, O., 2011. Thermal history of Mars inferred from orbital geochemistry of volcanic provinces. Nature 472, 338–341.

Bauer, S.J., Friedman, M., Handin, J., 1981. Effects of water-saturation on strength and ductility of three igneous rocks at effective pressures to 50 MPa and temperatures to partial melting. The 22nd U.S. Symposium on Rock Mechanics (USRMS), Cambridge, MA June 29 - July 2, 1981.
Benson, P.M., Thompson, A.B., Meredith, P.G., Vinciguerra, S., Young, R.P., 2007. Imaging slow failure in triaxially deformed Etna basalt using 3D acoustic-emission location and X-ray computed tomography. Geophys. Res. Lett. 34, L03303. doi:10.1029/2006GL028721.
Benson, P.M., Heap, M.J., Lavallée, Y., Flaws, A., Hess, K.-U., Selvadurai, A.P.S., Dingwell, D.B., Schillinger, B., 2012. Laboratory simulations of tensile fracture development in a volcanic conduit via cyclic magma pressurisation. Earth Planet. Sci. Lett. 349-350, 231–239.
Bieniawski, Z.T., 1989. Engineering Rock Mass Classifications. Wiley, New York, p. 251.
Black, B.A., Mittal, T., 2015. The demise of phobos and development of a martian ring system. Nat. Geosci. 8, 913–917.
Black, B.A., Manga, M., 2016. The eruptibility of magmas at tharsis and syrtis major on Mars. J. Geophys. Res. 121, 944–964.
Brace, W.F., Kohlstedt, D.L., 1980. Limits on lithospheric stress imposed by laboratory experiments. J. Geophys. Res. 85, 6248–6252.
Brantut, N., Heap, M.J., Meredith, P.G., Baud, P., 2013. Time-dependent cracking and brittle creep in crustal rocks: a review. J. Struct. Geol. 52, 17–43.
Byerlee, J.D., 1978. Friction of rocks. Pure Appl. Geophys. 116, 615–626.
Byrne, P.K., Holohan, E.P., Kervyn, M., van Wyk de Vries, B., Troll, V.R., Murray, J.B., 2013. A sagging-spreading continuum of large volcano structure. Geology 41, 339–342.
Cattermole, P., 1987. Sequence, rheological properties, and effusion rates of volcanic flows at alba Patera, Mars. J. Geophys. Res. 92, E553–E560.
Caristan, Y., 1982. The transition from high temperature creep to fracture in maryland diabase. J. Geophys. Res. 87, 6781–6790.
Carr, M.H., 1973. Volcanism on Mars. J. Geophys. Res. 78, 4049–4062.
Carr, M.H., 1979. Formation of martian flood features by release of water from confined aquifers. J. Geophys. Res. 84 (B6), 2995–3007.
Carr, M.H., 2000. Martian oceans, valleys, and climate. News Rev. Astron. Geophys. 41. doi:10.1046/j.1468-4004.2000.00320.x.
Carr, M.H., Head, J.W., 2010. Geologic history of Mars. Earth Planet. Sci. Lett. 294, 185–203.
Carr, M.H., Head, J.W., 2015. Martian surface/near-surface water inventory: Sources, sinks, and changes with time. Geophys. Res. Lett. 42, 726–732.
Clifford, S.M., 1993. A model for the hydrologic and climatic behavior of water on Mars. J. Geophys. Res. 98 (E6), 10973–11016.
Coleman, N.M., Dinwiddie, C.L., Casteel, K., 2007. High outflow channels on Mars indicate hesperian recharge at low latitudes and the presence of canyon lakes. Icarus 189, 344–361.
Cottrell, E., 2015. Global distribution of active volcanoes. In: Papale, P. (Ed.), Volcanic Hazards, Risks, and Disasters. Elsevier, pp. 1–14.
Crisp, J., 1984. Rates of magma emplacement and volcanic output. J. Volcanol. Geotherm. Res. 20, 177–211.
David, C., Wong, T.-f., Zhu, W., Zhang, J., 1994. Laboratory measurement of compaction-induced permeability change in porous Rocks: implications for the generation and maintenance of pore pressure excess in the crust. Pure Appl. Geophys. 143, 425–456.
Duclos, R., Paquet, J., 1991. High-temperature behaviour of basalts—role of temperature and strain rate on compressive strength and K_{IC} toughness of partially glassy basalts at atmospheric pressure. Int. J. Rock Mech. Mining Sci. Geomech. Abstracts 28, 71–76.
Evans, B., Fredrich, J.T., Wong, T.-f., 1990. The brittle-ductile transition in rocks: recent experimental and theoretical progress. In: Duba, A.G., Durham, W.B., Handin, J.W., Wang, H.F. (Eds.), The Brittle-Ductile Transition in Rocks. American Geophysical Union, Washington, D. C. doi:10.1029/GM056p0001.
Fuller, E.R., Head, J.W., 2003. Olympus Mons, Mars: detection of extensive preaureole volcanism and implications for initial mantle plume behavior. Geology 31, 175–178.
Greeley, R., Spudis, P.D., 1981. Volcanism on Mars. Rev. Geophys. 19, 13–41.
Green, D.H., Ringwood, A.E., 1967. The genesis of basaltic magmas. Contrib. Mineral. Petrol. 15, 103–190.
Griggs, D.T., Turner, F.J., Heard, H.C., 1960. Deformation of rocks at 500 to 800 °C. In: Griggs, D.T., Handin, J.W. (Eds.). In: Rock Deformation, 79. Geological Society of America Memoirs, pp. 39–104.
Grott, M., Hauber, E., Werner, S.C., Kronberg, P., Neukum, G., 2007. Mechanical modeling of thrust faults in the thaumasia region, Mars, and implications for the noachian heat flux. Icarus 186, 517–526.
Gudmundsson, A., 2002. Emplacement and arrest of dykes and sheets in central volcanoes. J. Volcanol. Geotherm. Res. 116, 279–298.
Gudmundsson, A., 2006. How local stresses control magma-chamber ruptures, dyke injections, and eruptions in composite volcanoes. Earth Sci. Rev. 79, 1–31.
Gudmundsson, A., 2011. Rock Fractures in Geological Processes. Cambridge University Press ISBN: 978-0-521-86392-6.
Hacker, B.R., Christie, J.M., 1991. Experimental deformation of a glassy basalt. Tectonophysics 200, 79–96.
Hauck, S.A., Phillips, R.J., 2002. Thermal and crustal evolution of Mars. J. Geophys. Res. 107. doi:10.1029/2001JE001801.
Head, J.W., Wilson, L., 1992. Magma reservoirs and neutral buoyancy zones on Venus: implications for the formation and evolution of volcanic landforms. J. Geophys. Res. 97, 3877–3903.
Head, J.W., Marchant, D.R., Ghatan, G.J., 2004. Glacial deposits on the rim of a hesperian-amazonian outflow channel source trough: mangala Valles, Mars. Geophys. Res. Lett. 31, L10701. doi:10.1029/2004GL020294.
Head, J.W., Wilson, L., Dickson, J., Neukum, G., 2006. The huygens-hellas giant dike system on Mars: implications for late noachian–early hesperian volcanic resurfacing and climatic evolution. Geology 34, 285–288.
Heap, M.J., Vinciguerra, S., Meredith, P.G., 2009. The evolution of elastic moduli with increasing damage during cyclic stressing of a basalt from Mt. Etna volcano. Tectonophysics 471, 153–160.
Heap, M.J., Baud, P., Meredith, P.G., Vinciguerra, S., 2011. Brittle creep in basalt and its application to time-dependent volcano deformation. Earth Planet. Sci. Lett. 307, 71–82.
Heap, M.J., Kennedy, B.M., 2016. Exploring the scale-dependent permeability of fractured andesite. Earth Planet. Sci. Lett. doi:10.1016/j.epsl.2016.05.004.
Hoek, E., Brown, E.T., 1980. Empirical strength criterion for rock masses. J. Geotech. Eng. Div. ASCE 106, 1013–1035.
Hoek, E., 1994. Strength of rock and rock masses. Int. Soc. Rock Mech. News J. 2 (2), 4–16.
Holland, G., Sherwood Lollar, B., Li, L., Lacrampe-Couloume, G., Slater, G.F., Ballentine, C.J., 2013. Deep fracture fluids isolated in the crust since the precambrian era. Nature 497, 357–360.
Hopper, J.P., Leverington, D.W., 2014. Formation of hrad vallis (Mars) by low viscosity lava flows. Geomorphology 207, 96–113.
Jaeger, J.C., Cook, N.G.W., Zimmerman, R., 2007. Fundamentals of Rock Mechanics. Blackwell Publishing ISBN: 978-0-632-05759-7.
Kieffer, H.H., Martin, T.Z., Peterfreund, A.R., Jakosky, B.M., 1977. Thermal and albedo mapping of Mars during the viking primary mission. J. Geophys. Res. 82, 4249–4291.
Klimczak, C., 2015. Limits on the brittle strength of planetary lithospheres undergoing global contration. J. Geophys. Res. 120, 2135–2151.
Kohlstedt, D.L., Evans, B., Mackwell, S.J., 1995. Strength of the lithosphere: constraints imposed by laboratory experiments. J. Geophys. Res. 100, 17587–17602.
Kohlstedt, D.L., Mackwell, S.J., 2010. Strength and deformation of planetary lithospheres. In: Watters, T.R., Schultz, R.A. (Eds.), Planetary Tectonics. Cambridge Univ. Press, New York, pp. 397–456.
Lavallée, Y., Benson, P.M., Heap, M.J., Hess, K.-U., Flaws, A., Schillinger, B., Meredith, P.G., Dingwell, D.B. (2013), Reconstructing magma failure and the degassing nework of dome-building eruptions, Geology, DOI: 10.1130/G33948.1.
Lillis, R.J., Dufek, J., Bleacher, J.E., Manga, M., 2009. Demagnetization of crust by magmatic intrusion near the arsia mons volcano: magnetic and thermal implications for the development of the tharsis province, Mars. J. Volcanol. Geotherm. Res. 185, 123–138.
MacKinnon, D.J., Tanaka, K.L., 1989. The impacted martian crust: Structure, hydrology, and some geologic implications. J. Geophys. Res. 94, 17359–17370.
Mackwell, S.J., Zimmerman, M.E., Kohlstedt, D.L., 1998. High-temperature deformation of dry diabase with application to tectonics on venus. J. Geophys. Res. 103, 975–984.
Martín-Torres, F.J., Zorzano, M.-P., Valentín-Serrano, P., Harri, A.-M., Genzer, M., Kemppinen, O., Rivera-Valentin, E.G., Jun, I., Wray, J., Madsen, M.B., Goetz, W., McEwen, A.S., Hardgrove, C., Renno, N., Chevrier, V.F., Mischna, M., Navarro-González, R., Martínez-Frías, J., Conrad, P., McConnochie, T., Cockell, C., Berger, G., Vasavada, A.R., Sumner, D., Vaniman, D., 2015. Transient liquid water and water activity at gale crater on Mars. Nat. Geosci. 8. doi:10.1038/NGEO2412.
McEwen, A.S., Malin, M.C., Carr, M.H., Hartmann, W.K., 1999. Voluminous volcanism on early Mars revealed in valles marineris. Nature 397, 584–586.
McGill, G.E., Squyres, S.W., 1991. Origin of the martian crustal dichotomy: evaluating hypotheses. Icarus 93, 386–393.
McGovern, P.J., Solomon, S.C., Smith, D.E., Zuber, M.T., Simons, M., Wieczorek, M.A., Phillips, R.J., Neumann, G.A., Aharonson, O., Head, J.W., 2002. Localized gravity/topography admittance and correlation spectra on Mars: implications for regional and global evolution. J. Geophy. Res. 107. doi:10.1029/2002JE001854.
McSween, H.Y., Labotka, T.C., Viviano-Beck, C.E., 2015. Metamorphism in the martian crust. Meteorit. Planet. Sci. 50, 590–603.
McSween, H.Y., Taylor, G.J., Wyatt, M.B., 2009. Elemental composition of the martian crust. Science 324, 736–739.
Mège, D., Masson, P., 1997. Tension fracturing at uranius Fossae, Mars. In: Conference Paper, 28th Annual Lunar and Planetary Science Conference, p. 931.
Mitchell, T.M., Faulkner, D.R., 2012. Towards quantifying the matrix permeability of fault damage zones in low porosity rocks. Earth Planet. Sci. Lett. 339-340, 24–31.
Montési, L., Zuber, M.T., 2003. Clues to the lithospheric structure of Mars from wrinkle ridge sets and localization instability. J. Geophys. Res. 108 (E6). doi:10.1029/2002JE001974.
Morgan, W.J., 1972. Deep mantle convection plumes and plate motions. Am. Assoc. Pet. Geol. Bull. 56, 203–213.
Nara, Y., Meredith, P.G., Yoneda, T., Kaneko, K., 2011. Influence of macro-fractures and micro-fractures on permeability and elastic wave velocities in basalt at elevated temperature. Tectonophysics 503, 52–59.
Neuffer, D.P., Schultz, R.A., 2006. Mechanisms of slope failure in valles Marineris, Mars. Quart. J. Eng. Geol. Hydrol. 39, 227–240.
Ojha, L., Wilhelm, M.B., Murchie, S.L., McEwen, A., Wray, J.J., Hanley, J., Massé, M., Chojnacki, M., 2015. Spectral evidence for hydrated salts in recurring slope lineae on Mars. Nat. Geosci. 8, 829–832.
Okubo, C.H., Tornabene, L.L., Lanza, N.L., 2011. Constraints on mechanisms for the growth of gully alcoves in gasa crater, Mars, from two-dimensional stability assessments of rock slopes. Icarus 211, 207–221.

Ougier-Simonin, A., Fortin, J., Guéguen, Y., Schubnel, A., Bouyer, F., 2011. Cracks in glass under triaxial conditions. Int. J. Eng. Sci. 49, 105–121.
Owen, T., Biemann, K., Rushneck, D.R., Biller, J.E., Howarth, D.W., Lafleur, A.L., 1977. The composition of the atmosphere at the surface of Mars. J. Geophys. Res. 82, 4635–4639.
Paterson, M.S., Wong, T.-f., 2005. Experimental Rock Deformation-The Brittle Field. Springer-Verlag Berlin Heidelberg ISBN: 978-3-540-24023-5.
Phillips, R.J., Zuber, M.T., Solomon, S.C., Golombek, M.P., Jakosky, B.M., Banerdt, W.B., Smith, D.E., Williams, R.M.E., Hynek, B.M., Aharonson, O., Hauck, S.A., 2001. Ancient geodynamics and global-scale hydrology on Mars. Science 291, 2587–2591.
Plescia, J.B., 1990. Recent flood lavas in the elysium region of Mars. Icarus 88, 465–490.
Plescia, J.B., 2003. Cerberus Fossae, Elysium, Mars: a source for lava and water. Icarus 164, 79–95.
Plescia, J.B., 2004. Morphometric properties of martian volcanoes. J. Geophys. Res. 109 (E3). doi:10.1029/2002JE002031.
Pola, A., Crosta, G.B., Fusi, N., Barberini, V., Norini, G., 2012. Influence of alteration on physical properties of volcanic rocks. Tectonophysics 566-567, 67–86.
Rocchi, V., Sammonds, P.R., Kilburn, C.R.J., 2004. Fracturing of etnean and vesuvian rocks at high temperatures and low pressures. J. Volcanol. Geotherm. Res. 132, 137–157.
Rodriguez, J.A.P., Sasaki, S., Kuzmin, R.O., Dohm, J.M., Tanaka, K.L., Miyamoto, H., Kurita, K., Komatsu, G., Fairén, A.G., Ferris, J.C., 2005. Outflow channel sources, reactivation, and chaos formation, xanthe Terra, Mars. Icarus 175, 36–57.
Rubin, A.M., 1995. Propagation of magma-filled cracks. Annu. Rev. Earth Planet. Sci. 23, 287–336.
Ruiz, J., Fernández, C., Gomez-Ortiz, D., Dohm, J.M., López, V., Tejero, R., 2008. Ancient heat flow, crustal thickness, and lithospheric mantle rheology in the amenthes region, Mars. Earth Planet. Sci. Lett. 270, 1–12.
Ruiz, J., McGovern, P.J., Jiménez-DÍaz, A., López, V., Williams, J.-P., Hahn, B.C., Tejero, R., 2011. The thermal evolution of Mars as constrained by paleo-heat flows. Icarus 215, 508–517.
Ruiz, J., 2014. The early heat loss evolution of Mars and their implications for internal and environmental history. Sci. Rep. 4. doi:10.1038/srep04338.
Rutter, E., 1986. On the nomenclature of mode of failure transitions in rocks. Tectonophysics 122, 381–387.
Schaefer, L.N., Kendrick, J.E., Oommen, T., Lavallée, Y., Chigna, G., 2015. Geomechanical rock properties of a basaltic volcano. Front. Earth Sci. 3 (29). doi:10.3389/feart.2015.00029.
Schultz, R.A., 1993. Brittle strength of basaltic rock masses with applications to venus. J. Geophys. Res. 98, 10883–10895.
Schultz, R.A., 1995. Limits on strength and deformation properties of jointed basaltic rock masses. Rock Mech. Rock Eng. 28, 1–15.
Schultz, R.A., Watters, T.R., 2001. Forward mechanical modeling of the amenthes rupes thrust fault on Mars. Geophys. Res. Lett. 28, 4659–4662.
Schultz, R.A., Okubo, C.H., Wilkins, S.J., 2006. Displacement-length scaling relations for faults on terrestrial planets. J. Struct. Geol. 28, 2182–2193.
Shimada, M., Yukutake, H., 1982. Fracture and deformation of silicate rocks at high pressures in a cubic press. Adv. Earth Planet. Sci. 12, 193–205.
Shimada, M., 1986. Mechanism of deformation in a dry porous basalt at high pressures. Tectonophysics 121, 153–173.
Shimada, M., Ito, K., Cho, A., 1989. Ductile behavior of a fine-grained porous basalt at room temperature and pressures to 3 GPa. Phys. Earth Planet. Inter. 55, 361–373.
Smith, D.E., Zuber, M.T., 1996. The shape of Mars and the topographic signature of the hemispheric dichotomy. Science 271, 184–188.
Smith, D.E., Zuber, M.T., Solomon, S.C., Phillips, R.J., Head, J.W., Garvin, J.B., Banerdt, W.B., Muhleman, D.O., Pettengill, G.H., Neumann, G.A., Lemoine, F.G., Abshire, J.B., Aharonson, O., Brown, C.D., Hauck, S.A., Ivanov, A.B., McGovern, P.J., Zwally, H.J., Duxbury, T.C., 1999. The global topography of Mars and implications for surface evolution. Science 284, 1495–1503.
Solomon, S.C., 1978. On volcanism and thermal tectonics on one-plate planets. Geophys. Res. Lett. 5, 461–464.
Solomon, S.C., Head, J.W., 1982. Evolution of the tharsis province of Mars: the importance of heterogeneous lithospheric thickness and volcanic construction. J. Geophys. Res. 87, 9755–9774.
Solomon, S.C., Head, J.W., 1990. Heterogeneities in the thickness of the elastic lithosphere of Mars: constraints on heat flow and internal dynamics. J. Geophys. Res. 95, 11073–11083.
Tanaka, K.L., 1986. The stratigraphy of Mars. J. Geophys. Res. 91 (B13), E139–E158.
Tillmann, J.E., Johnson, N.C., Guttorp, P., Percival, D.B., 1993. The martian annual atmospheric pressure cycle: years without great dust storms. J. Geophys. Res. 98, 10963–10971.
Turcotte, D.L., Willemann, R.J., Haxby, W.F., Norberry, J., 1981. Role of membrane stresses in the support of planetary topography. J. Geophys. Res. 86, 3951–3959.
Vinciguerra, S., Trovato, C., Meredith, P.G., Benson, P.M., 2005. Relating seismic velocities, thermal cracking and permeability in Mt. Etna and iceland basalts. Int. J. Rock Mech. Min. Sci. 42, 900–910.
Violay, M., Gibert, B., Mainprice, D., Evans, B., Dautria, J.-M., Azias, P., Pezard, P., 2012. An experimental study of the brittle-ductile transition of basalt at oceanic crust pressure and temperature conditions. J. Geophys. Res. 117 (B3). doi:10.1029/2011JB008884.
Violay, M., Gibert, B., Mainprice, D., Burg, J.-P., 2015. Brittle versus ductile deformation as the main control of the deep fluid circulation in oceanic crust. Geophys. Res. Lett. doi:10.1002/2015GL063437.
Wang, H., Richardson, M.I., 2015. The origin, evolution, and trajectory of large dust storms on Mars during Mars years 24-30 (1999-2011). Icarus 251, 112–127.
Warner, N., Gupta, S., Muller, J.-P., Kim, J.-R., Lin, S.-Y., 2009. A refined chronology of catastrophic outflow events in ares Vallis, Mars. Earth Planet. Sci. Lett. 288, 58–69.
Watters, T.R., McGovern, P.J., Irwin III, R.P., 2007. Hemispheres apart: the crustal dichotomy on Mars. Annu. Rev. Earth Planet. Sci. 35, 621–652.
Wilkins, S.J., Schultz, R.A., Anderson, R.C., Dohm, J.M., Dawers, N.H., 2002. Deformation rates from faulting at the tempe terra extensional province, Mars. Geophys. Res. Lett. 29, 311–314.
Wilkins, S.J., Schultz, R.A., 2003. Cross faults in extensional settings: stress triggering, displacement localization, and implications for the origin of blunt troughs at valles Marineris, Mars. J. Geophys. Res. 108 (E6). doi:10.1029/2002JE001968.
Wilson, L., Head, J.W., 1983. A comparison of volcanic eruption processes on Earth, Moon, Mars, io and venus. Nature 302, 663–669.
Wilson, L., Head, J.W., 1994. Mars: review and analysis of volcanic eruption theory and relationships to observed landforms. Rev. Geophys. 32, 221–263.
Wilson, L., Scott, E.D., Head, J.W., 2001. Evidence for episodicity in the magma supply to the large tharsis volcanoes. J. Geophys. Res. 106, 1423–1433.
Wilson, L., 2009. Volcanism in the solar system. Nat. Geosci. 2, 389–397.
Wong, T.-f., Baud, P., 2012. The brittle-ductile transition in porous rock: a review. J. Struct. Geol. 44, 25–53.
Wyatt, M.B., McSween, H.Y., 2002. Spectral evidence for weathered basalt as an alternative to andesite in the northern lowlands of Mars. Nature 417, 263–266.
Wyering, L.D., Villeneuve, M.C., Wallis, I.C., Siratovich, P., Kennedy, B., Gravely, D.M., Cant, J.L., 2014. Mechanical and physical properties of hydrothermally altered rocks, taupo volcanic zone, new zealand. J. Volcanol. Geotherm. Res. 288, 76–93.
Zimmerman, R.W., Bodvarsson, G.S., 1996. Hydraulic conductivity of rock fractures. Transp. Porous. Media 23, 1–30.
Zhu, W., Baud, P., Vinciguerra, S., Wong, T.-f., 2016. Micromechanics of brittle faulting and cataclastic flow in Mt. Etna basalt: micromechanics of deformation in basalt. J. Geophys. Res. doi:10.1002/2016JB012826.
Zuber, M.T., Solomon, S.C., Phillips, R.J., Smith, D.E., Tyler, G.L., Aharonson, O., Balmino, G., Banerdt, W.B., Head, J.W., Johnson, C.L., Lemoine, F.G., McGovern, P.J., Neumann, G.A., Rowlands, D.D., Zhong, S., 2000. Internal structure and early thermal evolution of Mars from Mars global surveyor topography and gravity. Science 287, 1788–1793.